Results in Engineering 32 (2026) 112792

Contents lists available at ScienceDirect

Results in Engineering

journal homepage: www.sciencedirect.com/journal/results-in-engineering

Research paper

Data-driven prediction of cold spray additive manufacturing via CFD-guided machine learning

Fatema Tuj Zohora [a], Jaehun Jeon [a], Semih Akin [a,b,*]

[a] Mechanical, Aerospace, and Nuclear Engineering Department, Rensselaer Polytechnic Institute, Troy, NY, 12180, USA
[b] Center for Smart Convergent Manufacturing Systems (CSCMS), Rensselaer Polytechnic Institute, Troy, NY, 12180, USA

ARTICLE INFO

Keywords:
Cold spray additive manufacturing (CSAM)
Computational fluid dynamics (CFD)
Artificial intelligence (AI)
Data-driven modeling
Machine learning

ABSTRACT

Cold spray additive manufacturing (CSAM) has emerged as a promising solid-state manufacturing technique for fabricating metallic components and functional coatings. However, experimentally predicting particle impact properties (e.g., impact velocity, impact temperature) and correlating them with deposition state remains challenging due to the complex interactions among process parameters, gas dynamics, and particle behavior during deposition. These characteristics play a critical role in determining deposition efficiency (DE) and the quality of the deposited material, thereby highlighting the need for predictive modeling frameworks. In this study, a computational-fluid dynamics (CFD)-guided machine learning framework is developed to correlate CSAM input parameters (i.e., gas pressure, gas temperature, particle size) with deposition state (i.e., deposition/no deposition) and DE. Three-dimensional CFD simulations are conducted under varying gas pressures, gas temperatures, and particle sizes based on a design of experiments (DoE) to generate a particle-level dataset. The generated dataset is then used to train machine learning (ML) models for both classification and regression analysis. Logistic Regression (LR), Support Vector Machine (SVM), Random Forest (RF), and Neural Network (NN) models are implemented for deposition state prediction, while Ridge Regression (RR) and Gaussian Process Regression (GPR) models are employed for DE (%) prediction, enabling a comparative evaluation of ML model performance. Among the classification models, SVM and RF achieved the highest deposition state prediction accuracy of $\sim 98.5\%$, while GPR demonstrated better agreement with the CFD-generated DE trends, achieving a testing R^2 of 0.896. The findings highlight the potential of CFD-driven ML approaches for improving deposition prediction in CSAM, with significant potential to advance data-driven process modeling and intelligent manufacturing.

1. Introduction

Cold spray additive manufacturing (CSAM) is a solid-state deposition process in which micron-scale particles (5–100 μm) are accelerated to high velocities (300–1200 m/s) and deposited onto a target substrate through high-strain rate plastic deformation [1,2]. Unlike fusion-based additive manufacturing (AM) methods, CSAM avoids melting and solidification-related issues, such as oxidation, grain growth, and phase transformations [3,4]. Owing to these advantages, CSAM has attracted remarkable attention in strategic fields (e.g., 3D-printing, sustainable repair, corrosion protection, surface functionalization), with growing adoption across aerospace, automotive, energy, and advanced manufacturing sectors [5,6].

The CSAM process is primarily governed by particle impact conditions, particularly particle impact velocity (v_{imp}) and temperature (T_{pi}). Deposition occurs only when the v_{imp} exceeds a critical velocity (v_{cr}) [7]. Since the critical velocity is strongly influenced by both feedstock (powder) material properties and processing conditions, process parameters (e.g., gas pressure, gas temperature, particle size, spray angle, nozzle geometry) play an important role in determining the overall deposition behavior in CSAM [8–10]. However, these parameters are strongly interrelated and can significantly influence the gas flow behavior and particle impact conditions. As a result, modeling and optimizing the CSAM process remain complex and challenging tasks. Although several empirical equations and semi-analytical models have been proposed to estimate particle impact behavior and deposition conditions [11], these approaches remain limited to fully capture the complex multi-physics interactions governing the CSAM process.

In this context, numerical modeling of CSAM provides a powerful tool for understanding particle acceleration, impact behavior, and deposition mechanisms under various processing conditions without the need for extensive experimental trial-and-error. In particular, computational fluid dynamics (CFD) is an important tool for investigating flow behavior, particle acceleration, and particle flow dynamics in CSAM [9,12].

* Corresponding author.
E-mail address: akins@rpi.edu (S. Akin).

https://doi.org/10.1016/j.rineng.2026.112792
Received 30 June 2026; Received in revised form 1 September 2026; Accepted 2 September 2026
Available online 7 September 2026

Nomenclature

Symbols

A_p	Particle cross-sectional area (m^2)
C_D	Drag coefficient
C_p	Specific heat capacity ($J/(kg \cdot K)$)
E	Total energy per unit mass
k_{eff}	Effective thermal conductivity
m_p	Particle mass (kg)
p	Static pressure (Pa)
q	Heat flux
T	Temperature (K)
T_m	Particle melting temperature (K)
T_{pi}	Particle impact temperature (K)
$\vec{u}$	Gas velocity vector (m/s)
$\vec{v}_p$	Particle velocity vector (m/s)
v_{cr}	Critical velocity (m/s)
v_{imp}	Particle impact velocity (m/s)

Greek letters

μ_{eff}	Effective viscosity
ρ	Gas density (kg/m^3)
ρ_p	Particle density (kg/m^3)
τ_{eff}	Effective viscous stress tensor

Abbreviations

ANN	Artificial Neural Network
CAE	Convolutional Autoencoder
CFD	Computational Fluid Dynamics
CNN	Convolutional Neural Network
CS	Cold spray
CSAM	Cold Spray Additive Manufacturing
DE	Deposition Efficiency
DNN	Deep neural network
DPM	Discrete Phase Model
DT	Decision Tree
GB	Gradient boosting
GPR	Gaussian Process Regression
KNN	k-nearest neighbors
LR	Logistic Regression
ML	Machine learning
MLP	Multilayer perceptron
NN	Neural Network
PSO	Particle swarm optimization
RF	Random Forest
RR	Ridge Regression
RMSE	Root mean square error
SVM	Support Vector Machine
SVR	Support Vector Regression
XGBoost	Extreme Gradient Boosting

Although CFD provides detailed insights into gas flow characteristics and particle impact conditions, it is often computationally expensive and time-consuming, particularly for large parametric studies and process optimization tasks. As such, this underscores the need for efficient predictive frameworks capable of rapidly estimating deposition behavior and process outcomes in CSAM, particularly by correlating inlet process conditions (i.e., gas pressure, gas temperature, particle size) with particle acceleration, impact behavior, deposition efficiency (DE), and overall coating quality.

Data-driven modeling via machine learning (ML) has gained attention as a faster approach for process prediction and optimization in CSAM. ML models can learn the relationships between process parameters and deposition behavior from training datasets, enabling rapid prediction and optimization of CSAM process outcomes under varying operating conditions. A summary of recent ML-based studies in CSAM is provided in Table 1. This body of work has demonstrated the strong potential of ML-driven approaches for accelerating process optimization, reducing computational cost, and improving the overall understanding of complex deposition phenomena in CSAM. Despite these advances, the current literature lacks comprehensive ML frameworks capable of directly correlating key process parameters (i.e., gas pressure, gas temperature, particle size) with deposition outcomes, including deposition state (i.e., deposition/no deposition) and DE. In particular, the development of robust predictive models that can accurately capture the coupled and often nonlinear effects of process parameters on deposition behavior remains largely unexplored. Addressing this gap is essential for enabling rapid process design, improving predictive capability, and facilitating the broader adoption of data-driven optimization strategies in CSAM.

This study aims to address this gap by developing a CFD-guided machine learning framework for predicting deposition state and DE in CSAM under varying processing conditions, as illustrated in Fig. 1. First, three-dimensional (3D) CFD simulations are developed based on a design of experiments (DoE), considering a comprehensive range of gas pressure, gas temperature, and particle sizes to generate particle-level dataset describing gas flow behavior and particle impact conditions. Subsequently, the generated dataset is used to train ML models for the classification of deposition state (i.e., deposition/no deposition), as well as regression-based prediction of DE. Multiple ML models are compared to evaluate their prediction accuracy and robustness. The proposed framework provides a rapid and computationally efficient approach for predicting the CSAM process across a wide range of process conditions. Overall, this study advances the CSAM field through the following key contributions:

(i) Process-structure-property relationships between key CSAM process parameters and particle impact behavior through 3D CFD simulations.
(ii) Systematic implementation and comparison of multiple ML models for both classification (deposition/no deposition) and regression-based prediction tasks.
(iii) Development of a rapid and computationally efficient framework that reduces reliance on costly CFD simulations and experimental trial-and-error testing.

2. Methods

2.1. Computational modeling

2.1.1. Computational domain and boundary conditions

A three-dimensional (3D) computational domain was developed to model gas-particle flow behavior in the CSAM process. The geometry was based on the converging-diverging (CD) nozzle used in the low-pressure CSAM experimental setup [29]. The computational domain and its dimensions are illustrated in Fig. 2(a). The nozzle dimensions were measured from a commercial low-pressure CSAM system (i.e., *Titomic D523*) and adopted in the CFD simulations. The nozzle consists of a 10 mm inlet diameter, a 2.5 mm throat diameter, and a diverging section that expands to a 5 mm exit diameter. To capture the evolution of the jet after exiting the nozzle, an extended downstream atmospheric region was included, allowing the flow to expand and develop prior to particle impact. Spherical copper (Cu) particles were considered as the feedstock material, while aluminum was used as the substrate.

Fig. 2(b) presents the boundary conditions applied to the computational domain. The nozzle inlet was specified using prescribed pressure and temperature conditions, whereas the powder injection inlet and the outer atmospheric boundaries were modeled as pressure-outlet boundaries [30]. Particles were injected through the powder inlet located upstream of the nozzle throat region. The particle injection direction was defined normal to the powder inlet surface with an initial injection

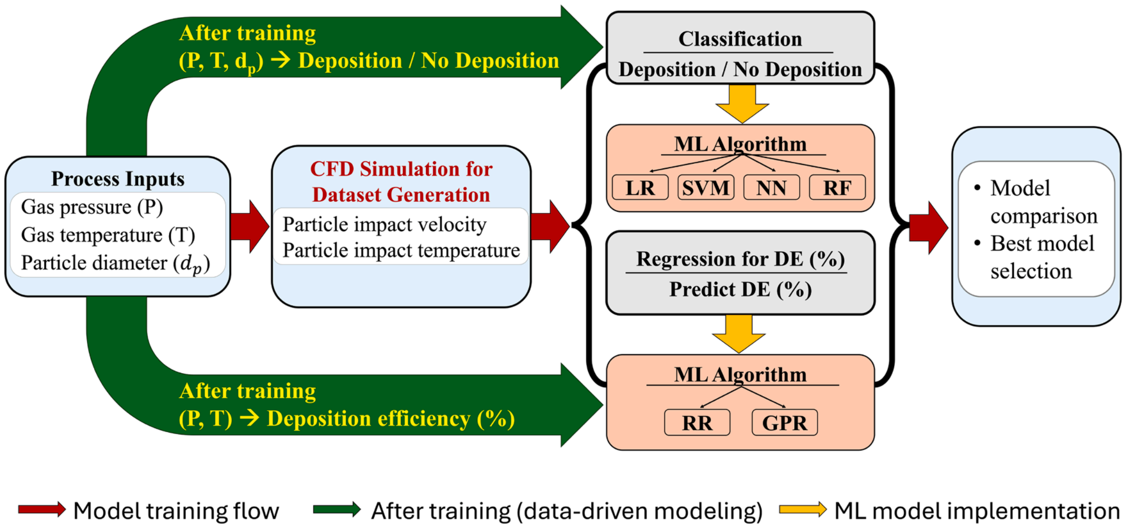

Fig. 1. CFD-driven machine learning framework developed to predict deposition state and deposition efficiency in CSAM.

velocity of 5 m/s. A total particle mass flow rate of 1.5×10^{-4} kg/s was used throughout the simulations. A flat substrate was positioned downstream of the nozzle at a stand-off distance of 30 mm from the nozzle exit. The substrate was placed normal to the nozzle centerline to investigate particle impact behavior and dispersion characteristics under different operating conditions. All nozzle walls and substrate surfaces were treated as stationary no-slip walls.

2.1.2. Continuous phase (gas flow)

Air and helium (He) were considered as driving gases in the simulations. Air was selected owing to its economic and energy-efficiency over nitrogen (N_2) and He, as well as the growing interest in air-based cold spray applications [31]. Notably, air and N_2 have similar molecular weights and thermodynamic properties and therefore exhibit comparable gas-flow characteristics under identical process conditions and nozzle geometries [32]. Accordingly, the trends observed for air are expected to be broadly applicable to N_2. Helium was also considered because of its low molecular weight and high speed of sound, which enable substantially higher gas and particle velocities and thus provide a useful comparison for evaluating the influence of driving-gas properties on particle acceleration and deposition behavior.

The continuous gas flow inside the nozzle and the surrounding atmospheric domain was modeled as a steady-state, compressible, turbulent flow using a pressure-based solver. The gas phase behavior was governed by the compressible Navier–Stokes equations representing the conservation of mass, momentum, and energy. The governing equations used for the continuous phase are expressed as follows [33]:

Continuity equation:

$$\nabla \cdot (\rho \mathbf{u}) = 0 \tag{1}$$

Momentum equation:

$$\nabla \cdot (\rho \mathbf{u} \otimes \mathbf{u}) = -\nabla p + \nabla \cdot \boldsymbol{\tau}_{eff} \tag{2}$$

Energy equation:

$$\nabla \cdot [\mathbf{u}(\rho E + p)] = \nabla \cdot (\boldsymbol{\tau}_{eff} \mathbf{u}) - \nabla \cdot \mathbf{q} \tag{3}$$

where ρ is the gas density, $\mathbf{u}$ is the velocity vector, p is the static pressure, and E represents the total energy per unit mass. The effective viscous stress tensor and heat flux are defined as:

$$\boldsymbol{\tau}_{eff} = \mu_{eff}\left[\nabla \mathbf{u} + (\nabla \mathbf{u})^T\right] - \frac{2}{3}\mu_{eff}(\nabla \cdot \mathbf{u})\mathbf{I} \tag{4}$$

$$\mathbf{q} = -k_{eff}\nabla T \tag{5}$$

where μ_{eff} and k_{eff} denote the effective viscosity and effective thermal conductivity, respectively.

The gas phase simulations were performed using the realizable k–ε turbulence model [34] to capture the turbulent characteristics of the supersonic flow. This particular model was selected because of its capability in predicting rapidly strained and highly accelerated flows commonly observed in cold spray nozzles. The governing equations were solved using a coupled pressure-velocity scheme with second-order spatial discretization for pressure, momentum, turbulence quantities, and energy equations. The numerical solution was considered converged when the residuals of the governing equations dropped below 10^{-6}.

2.1.3. Discrete phase (particle flow)

Spherical Cu particles were considered in the simulations with a density of 8,978 kg/m^3 and a specific heat capacity of 381 J/(kg·K). The particle size distribution followed the Rosin–Rammler distribution model with minimum, mean, and maximum particle diameters of 5 μm, 36 μm, and 44 μm, respectively [35]. This distribution was selected to represent the realistic powder characteristics commonly used in cold spray processes.

The discrete-phase (particle) motion was modeled using a Lagrangian framework [34] based on the force-balance equations (i.e., Newton's second law).

$$m_p \frac{d\vec{v}_p}{dt} = C_D \rho\left(\vec{v} - \vec{v}_p\right)\left|\vec{v} - \vec{v}_p\right|\frac{A_p}{2} + \vec{g}\frac{(\rho_p - \rho)}{\rho_p} + \vec{F} \tag{6}$$

where m_p, ρ_p, and $\vec{v}_p$ represent the particle mass, density, and velocity, respectively. A_p denotes the particle cross-sectional area, assumed circular for spherical particles. C_D is the drag coefficient, while $\vec{F}$ accounts for external forces acting on the particles during transport within the gas flow field.

The deposition state (i.e., deposition/no deposition) of particles was evaluated using the critical velocity (v_{cr}) criterion. A particle was considered deposited when the particle impact velocity exceeded the v_{cr}. The critical velocity was estimated using the empirical relationship proposed by Schmidt et al. [36], which has also been used in recent studies [37]:

$$v_{cr} = 0.64\sqrt{\left(\frac{16\sigma_{TS}}{\rho_p(T_m - 293)} + C_p\right)(T_m - T_{pi})} \tag{7}$$

where σ_{TS} is the ultimate tensile strength, T_m is the melting point of particles, C_p is the specific heat capacity of the particles, and T_{pi} is the particle impact temperature.

Table 1
Overview of ML methods used in CSAM and their main findings.

References	ML Method	Application	Key Findings	Year
Falco et al. [13]	SVR, ANN	Prediction of particle velocity and temperature using CFD-based surrogate models	SVR accurately predicted particle velocity and temperature ($R^2 \approx 0.98$); SHAP showed that particle diameter and gas temperature strongly influence the predictions.	2026
Xia et al. [14]	RF, Extra Trees, XGBoost	Prediction of residual stress distribution	Extra Trees achieved highest accuracy ($R^2 \approx 0.995$) and reproduced FEM stress fields while reducing computation time.	2026
Afsharnia and Butt [15]	ANN, CNN, GPR, SVM, RF, GB, Hybrid ML (Physics-informed)	AI/ML applications in CSAM.	Identified four AI/ML research domains in CSAM and emphasized the need for physics-informed models	2025
Citarella et al. [16]	GPR, Bilayer NN, SVR, DT	Prediction of particle flattening and penetration depth on polymer substrates	GPR achieved the lowest RMSE for flattening (≈ 3.9), while the bilayer NN showed best performance for penetration depth (≈ 2.3).	2025
Perna et al. [17]	DT, NN, GPR	Prediction of flattening and penetration depth based on powder properties	Particle yield strength governed flattening; density primarily controlled penetration depth.	2025
Eberle et al. [18]	KNN, RF, GB, NN	Prediction of DE across broad CS parameters	GB and NN achieved RMSE $< 6\%$; gas temperature showed dominant nonlinear influence on DE.	2025
Falco et al. [19]	DNN	Prediction of single-track and 3D deposit geometry	DNN models enabled fast and accurate geometry prediction, improving CSAM toolpath planning.	2025
Wang et al. [20]	Regression-based Surrogate Model	Spatial distribution, impact velocity, and temperature prediction	Two-stage ML closely matched CFD results while significantly reducing computational cost.	2025
Hamrani et al. [21]	Two-stage ML and Bayesian Optimization	DE optimization	Combined classification and regression with Bayesian optimization to identify optimal process parameters.	2025
Savangouder et al. [22]	MLP and PSO	Prediction of input process parameters for desired spray deposit profile	PSO-MLP inverse model reliably predicted feasible process parameters despite nonlinear mapping.	2024
Eberle et al. [23]	SVR and NN	Particle velocity distribution and DE prediction	Predicted average velocity (RMSE $\approx$ 41m/s) and DE (RMSE $\approx 3.2\%$); single-particle prediction was limited by plume stochasticity.	2024
Eberle et al. [24]	RF, SVM, ANN	Porosity prediction in cold spray coatings	Predicted porosity with average deviation of 0-2% from experimental values after dataset optimization.	2024
Aparco et al. [25]	EM-based Regression Model	Prediction of tensile and compressive residual stresses	Accurately predicted residual stresses (R^2 up to 0.968); thermal conductivity strongly influenced high-stress regimes.	2024
Lee et al. [26]	CAE, CNN	Powder flow monitoring	Two-stage interpretable DL model achieved 95% accuracy and improved noise-robust diagnostics.	2024
Wang et al. [27]	ANN	Critical velocity prediction	Demonstrated that mechanical properties had stronger influence than thermal properties; ANN achieved $>95\%$ prediction accuracy.	2021
Canales et al. [28]	LR, SVM, kNN, RF, Polynomial Regression	Deposition window identification and DE prediction	Classification models better predicted DE from unseen data.	2020

To capture the deposition state of the particles, the substrate boundary was defined using a trap boundary condition.

2.1.4. Grid independence test

Fig. 2(b) illustrates the computational mesh employed in the modeling. An unstructured mesh was generated with local refinement in critical regions, including the nozzle throat, powder injection inlet, and nozzle exit, to accurately resolve the strong flow gradients associated with the supersonic jet. A comparatively coarser mesh was employed in the far-field atmospheric region to reduce computational cost while maintaining numerical accuracy. A grid independence study was conducted using three mesh densities consisting of 7,530,234, 8,737,831, and 9,542,709 elements. The axial gauge-pressure distribution along the nozzle centerline was selected as the evaluation metric. As shown in Fig. 2(c), the predicted pressure profiles exhibited negligible differences among the three mesh configurations, indicating mesh-independent results. Consequently, the mesh containing 7,530,234 elements was selected for all subsequent simulations, as it provided an optimal balance between computational efficiency and solution accuracy. This mesh configuration enabled accurate resolution of the gas-flow field, including key flow features such as shock-wave formation and expansion characteristics, as illustrated in Fig. 2(d)–(e).

2.1.5. Model validation

The numerical model was first validated through comparison with experimental temperature measurements obtained under representative CSAM conditions. A polyurethane foam was used as an insulating target and positioned at a stand-off distance of 30 mm from the nozzle. Air was sprayed onto the foam without powder injection at various gas temperatures (i.e., 200 °C, 300 °C, 400 °C) under an operating pressure of 6 bar (gauge). The maximum surface temperature of the foam was measured using an infrared (IR) camera (*FLIR C8*) after steady-state thermal conditions were reached. Details of the experimental measurement procedure are provided in the Supporting Information (see Figure S1). For the CFD simulations, a monitoring plane was defined 30 mm downstream of the nozzle exit, corresponding to the experimental measurement location. The maximum temperature on this plane was extracted under the same operating conditions and compared with the experimental results. As shown in Fig. 2(f), the numerical predictions were in good agreement with the experimental measurements. The CFD model successfully captured the trend of increasing target surface temperature with increasing gas temperature, with deviations ranging from 2.4% to 26.2%. Notably, the deviation decreased at higher gas temperatures, reaching its minimum value at 400 °C. This trend is likely attributed to the increased dominance of forced convective heat transfer at higher gas temperatures, which is more accurately represented by the governing assumptions and boundary conditions employed in the CFD model. In contrast, at lower gas temperatures, additional uncertainties associated with heat losses would become more significant relative to the overall temperature rise, leading to larger deviations.

The numerical model was further validated by comparing the CFD predicted gas-density contours with the experimental Schlieren imaging results reported by Ning et al. [38], as shown in Fig. 2(g). Since the nozzle geometry and overall flow configuration employed in their study closely resemble those considered in the present work, the published Schlieren images were used for validation of the simulated flow field. In the reference study, the flow field was visualized at a gas temperature of 300 ˚C and a nozzle inlet stagnation pressure of 0.8 MPa (absolute), corresponding to a gauge pressure of 0.7 MPa (7 bar). Accordingly, a CFD density contour generated under comparable operating conditions was selected for comparison. To ensure consistency with the experimental conditions reported by Ning et al. [38], nitrogen (N_2) was used as the driving gas in the CFD simulations for this validation case, which considered a free jet flow without substrate impingement.

Fig. 2(g) compares the CFD-predicted density contour with the experimental Schlieren image reported by Ning et al. [38]. A comparable qualitative agreement was observed between the numerical and experimental results. In both cases, the jet underwent rapid expansion upon exiting the nozzle, followed by the formation of characteristic diamond shock structures along the jet centerline. The CFD results successfully captured the alternating high and low-density regions visible in the Schlieren image, with comparable locations of the shock cells. Although minor differences were observed in the sharpness and intensity of certain flow features, the CFD model accurately captured the dominant flow structures and density distribution within the supersonic free jet, providing further confidence in the validity of the numerical framework.

2.2. Data-driven modeling

2.2.1. Dataset

To develop the data-driven models, a structured dataset was generated using CFD simulations based on a full-factorial design of experiments (DoE) as given in Table 2. The dataset was designed to capture the influence of key process parameters on particle behavior and deposition characteristics. In this study, gas pressure, gas temperature, and particle diameter were considered as the primary input variables, as they directly affect particle acceleration and impact dynamics. These parameters were systematically varied within the operating ranges defined in the computational model to generate a diverse set of simulation cases. For each case, particle impact conditions at the substrate were extracted from the CFD results. A total of 56 CFD simulation cases were performed using both air and He as carrier gases to investigate their effects on particle acceleration, impact behavior, and deposition performance in the CSAM process.

For data-driven modeling, the 28 He-based simulations were selected because helium spray generated a broader range of particle impact velocities and deposition efficiencies than air, resulting in a more diverse and representative dataset for ML model development. These simulations produced a particle-level dataset comprising 18,051 individual particle-impact records, including impact velocity (υ_{imp}) and impact temperature (T_{pi}). To assess ML models and avoid overfitting, the dataset was randomly divided into training and testing subsets, with 80% of the data allocated for training and the remaining 20% used for independent testing. Hence, the resulting dataset served as the foundation for training and evaluating the ML models developed for deposition state classification and DE prediction.

2.2.2. Classification of deposition state

To predict the deposition state (i.e., deposition/no deposition), each particle was labeled based on the critical velocity (υ_{cr}) defined in Eq. 7. For each simulation case, the particle impact velocity obtained from the CFD results was compared with the corresponding υ_{cr}. Cases in which the particle impact velocity exceeded υ_{cr} were labeled as successful deposition, whereas those with impact velocities below the critical velocity threshold were classified as non-deposition. This procedure resulted in a total of 18,051 labeled data points for the classification study. The labeling strategy is consistent with the fundamental principles of CSAM, where particle adhesion is governed by the ability of the impacting particle to exceed the minimum velocity required to induce sufficient plastic deformation and promote interfacial bonding upon impact.

To capture the relationship between the process parameters and deposition state, multiple ML classification models were implemented and compared (see Fig. 1). Logistic Regression (LR), Support Vector Machine (SVM), Random Forest (RF), and Neural Network (NN) models were selected to evaluate their predictive capability under different decision boundary characteristics. Additional details regarding the theoretical foundations and implementation of these algorithms can be found in Refs. [39–41]. LR was used as an interpretable baseline model, while SVM was included to capture nonlinear separation behavior between deposition and no deposition regions. In addition, RF was implemented to account for feature interactions and nonlinear relationships, whereas the NN model was used to learn complex patterns from the CFD-generated dataset.

2.2.3. Regression analysis for deposition efficiency

Regression models were developed to predict DE as a continuous response variable across a range of CSAM process conditions. Gas pressure and gas temperature were selected as the input variables due to their dominant influence on gas dynamics, particle acceleration, and deposition behavior. The CFD-generated dataset was used to train the regression models, enabling them to learn the relationships between process parameters and the resulting DE values. To achieve this, multiple regression models were implemented and compared. In particular, Ridge Regression (RR) [42] and Gaussian Process Regression (GPR) [43] models were selected to evaluate their performance for DE prediction. RR was chosen because of its stability and effectiveness in handling correlated input variables, while GPR was included due to its capability to capture nonlinear relationships and provide smooth predictive behavior for relatively small datasets [42,43].

3. Numerical modeling results and discussions

3.1. Gas flow characteristics

Fig. 3(a–b) present the CFD-predicted gas velocity contours within the nozzle and the downstream atmospheric region under various operating conditions. Fig. 3(a) illustrates the effect of inlet gas pressure (4, 7, and 10 bar) at a constant inlet temperature of 400 ˚C, while Fig. 3(b) shows the effect of inlet gas temperature (100, 300, and 400 ˚C) at a constant inlet pressure of 10 bar. The corresponding static pressure and temperature contour distributions for these operating conditions are provided in the Supporting Information (see Figure S2). A common velocity scale is used across all cases to facilitate direct comparison of the gas flow characteristics. In addition, enlarged views of the flow field between the nozzle exit and the substrate are included to provide a clearer visualization of the gas jet development in the particle impact region. These contour plots provide insight into the evolution of the gas flow field and the influence of processing parameters on gas acceleration, expansion behavior, and downstream jet characteristics, which ultimately

Table 2
Factors, levels, and responses in the design of experiments (DoE).

Factors	Levels	Response
Gas pressure (bar)	4, 5, 6, 7, 8, 9, 10	Particle impact velocity, v_{imp} (m/s)
Gas temperature (°C)	100, 200, 300, 400	Particle impact temperature, T_{pi} (°C)
Particle diameter (µm)	Rosin–Rammler distribution ($d_{\min} = 5\ \mu$m, $d_{mean} = 36\ \mu$m, $d_{\max} = 44\ \mu$m)	–

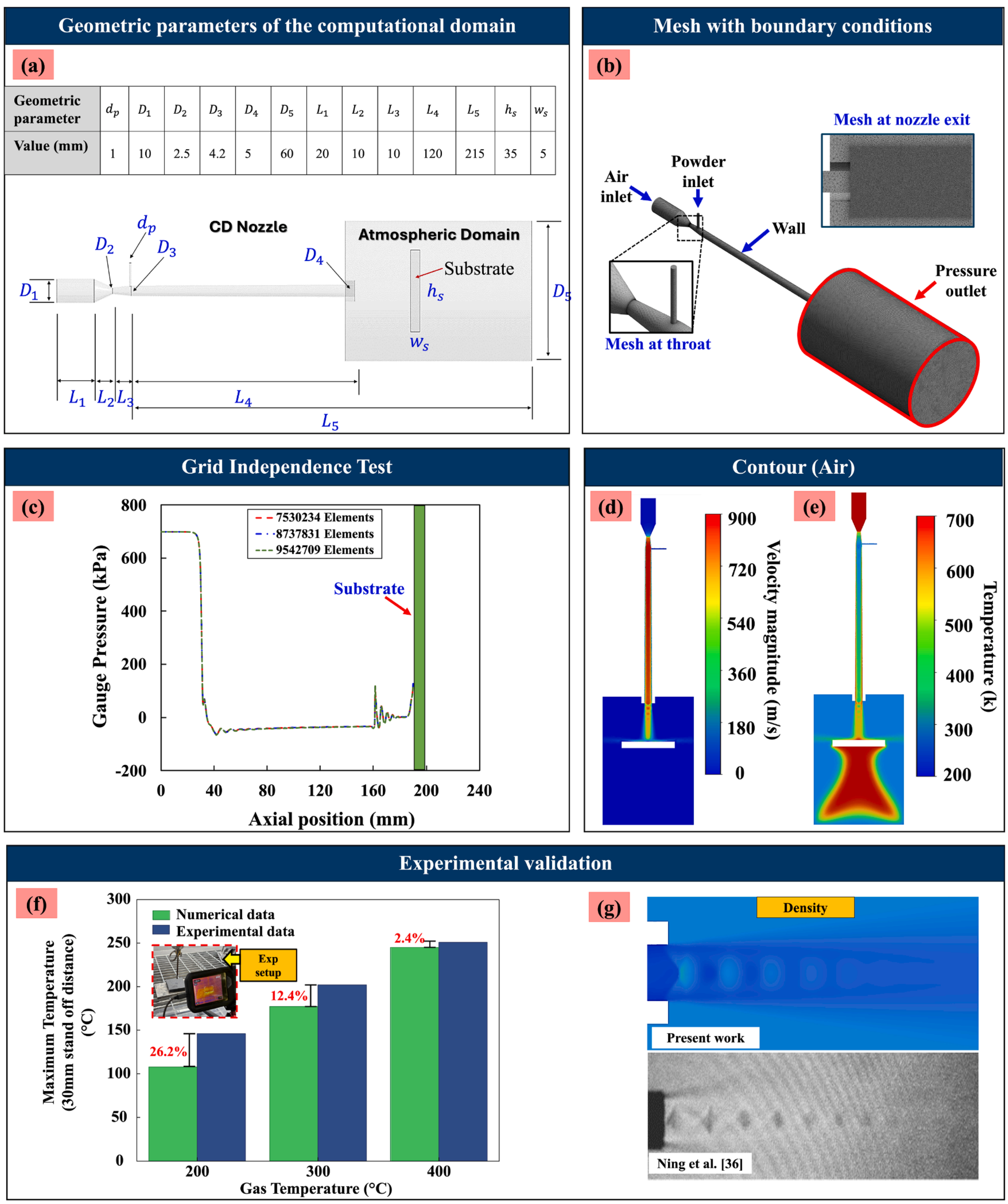

Fig. 2. Computational setup, model validation, and predicted flow-field characteristics of the continuous gas phase: (a) Computational domain and geometric dimensions; **(b)** Mesh configuration and boundary conditions; **(c)** Grid-independence analysis; **(d)** Velocity contour; **(e)** Temperature contour; **(f)** Experimental validation results; and **(g)** Comparison of the predicted density contours with the Schlieren-based flow-field observations reported by Ref. [38].

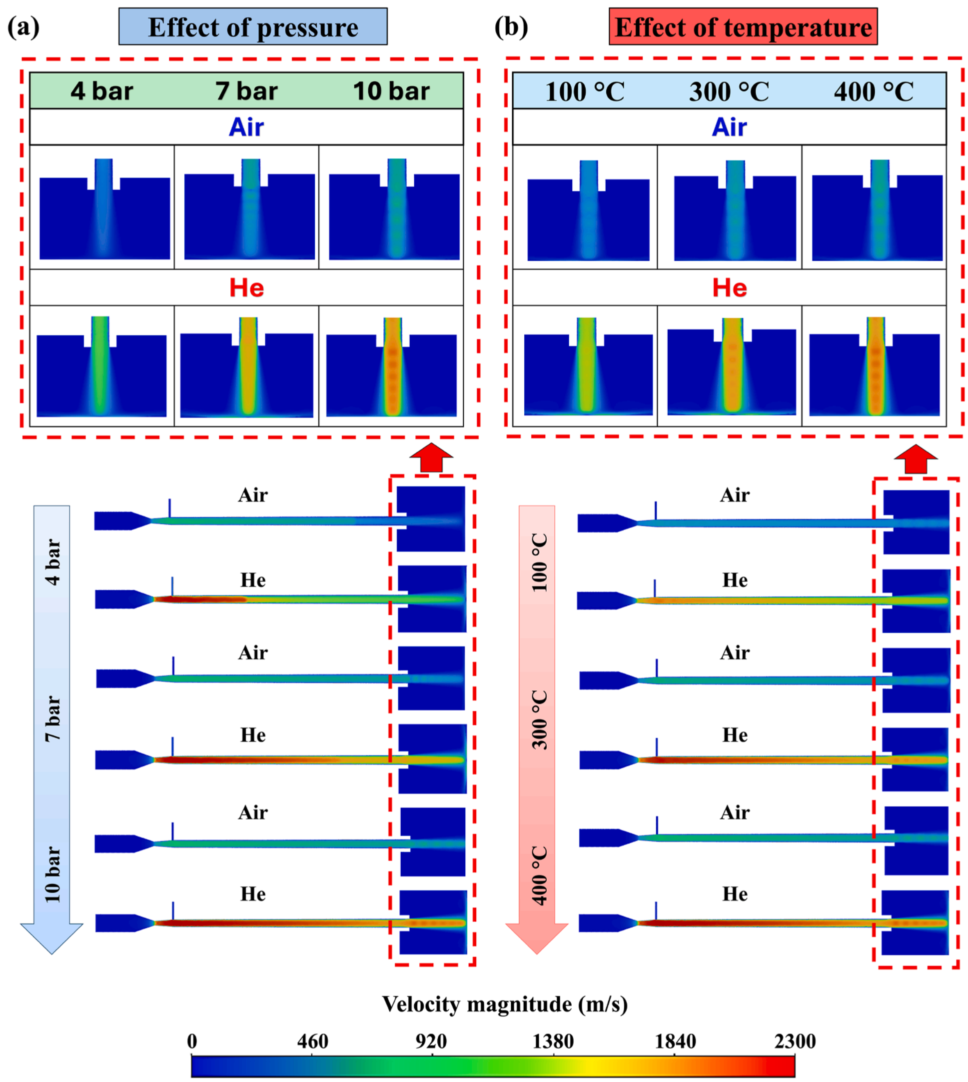

Fig. 3. Effect of operating conditions on the gas velocity field predicted by CFD: (a) influence of inlet gas pressure (4, 7, and 10 bar) at a constant inlet temperature of 400 °C; **(b)** influence of inlet gas temperature (100, 300, and 400 °C) at a constant inlet pressure of 10 bar.

govern particle transport and impact dynamics during the CSAM process.

Fig. 3(a) shows that the gas velocity field is strongly influenced by the inlet pressure. As the inlet pressure increases from 4 to 10 bar, the gas undergoes greater expansion and acceleration within the nozzle, resulting in progressively higher gas velocities throughout the flow domain. This effect is particularly pronounced near the nozzle exit. The enlarged contour views further illustrate that increasing pressure not only raises the peak gas velocity but also increases the spatial extent of the high-velocity flow field, thereby enhancing the momentum available for particle acceleration. A comparison of the two carrier gases (air and He) reveals significant differences in the velocity distributions across all operating conditions. The air cases produced lower gas velocities throughout the flow field. In contrast, the He cases exhibit a substantially larger high-velocity region, particularly within the nozzle and near the nozzle exit. This trend remains consistent across the entire pressure range investigated. These differences are also evident in the enlarged views, where considerably higher velocity levels are observed in the region between the nozzle exit and the substrate for He compared to air. The contour distributions further indicate a substantial increase in peak gas velocity when helium is used as the carrier gas. This behavior can be attributed to the lower molecular weight and density of helium [44], which promotes greater gas acceleration during nozzle expansion and results in a higher-velocity supersonic jet.

A similar trend is observed with increasing inlet gas temperature, as shown in Fig. 3(b). Increasing the inlet temperature from 100 °C to 400 °C enhances the gas velocity for both carrier gases, resulting in a broader high-velocity region throughout the flow field. This behavior is consistent with the ideal gas law ($P = \rho RT$), where increasing temperature raises the thermal energy of the gas molecules, promoting greater gas expansion and acceleration through the nozzle. Compared with the lower-temperature cases, the higher-temperature conditions exhibit a pronounced expansion of the high-velocity region between the nozzle exit and the substrate. This trend is further evident in the enlarged views, which show progressively higher velocity levels as the inlet temperature increases.

3.2. Particle flow characteristics

Fig. 4 presents the particle dispersion patterns on the substrate and the corresponding particle impact velocity distributions under varying CSAM gas pressure and temperature conditions for both air and helium carrier gases. Additional particle dispersion plots for the full set of operating conditions are provided in Figures S3-S4 (Supporting Information).

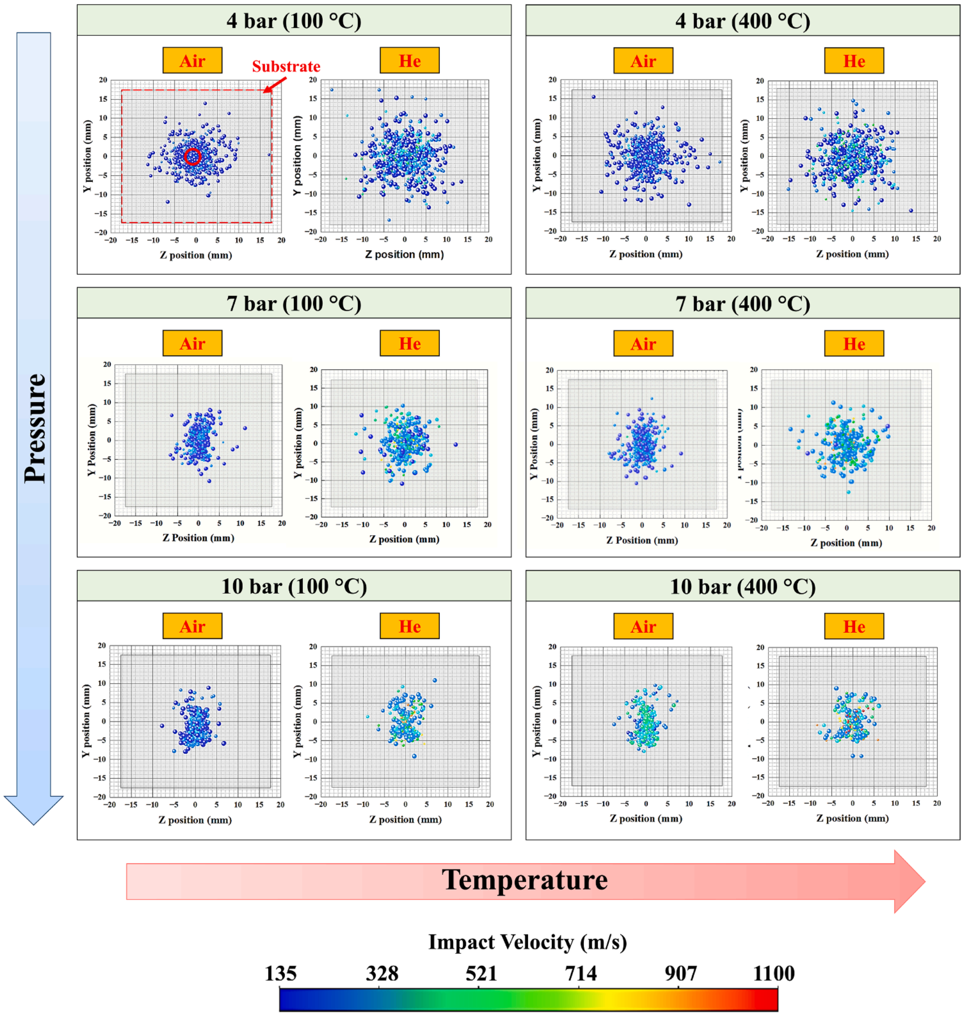

Fig. 4. Effect of gas temperature and pressure on particle dispersion and impact velocity distribution.

These results provide further insight into the effects of carrier gas type and processing parameters on particle trajectories, dispersion behavior, and impact velocities. In these plots, particle color denotes the impact velocity, while particle size represents the injected particle diameter distribution. Independent of the process gas, particle impact velocity increased with increasing gas pressure and temperature, consistent with ideal gas law behavior. Higher gas pressures and temperatures increase the gas expansion ratio and flow velocity within the nozzle, resulting in greater momentum transfer to the particles and, consequently, higher impact velocities.

At lower operating conditions (i.e., 4 bar and 100 °C), the particles exhibited relatively low impact velocities and a comparatively broad dispersion pattern downstream of the nozzle for both air and He cases (Fig. 4, top panel). Under these conditions, particle acceleration within the nozzle is limited, resulting in lower particle momentum upon substrate impact. Notably, although He produced substantially higher particle impact velocities than air, a greater degree of particle dispersion was also observed. This behavior is likely attributed to the lower density of He, which promotes more rapid gas expansion upon exiting the nozzle and increases particle sensitivity to the surrounding flow field. As a result, particles carried by He experience greater radial spreading despite their higher velocities, leading to a broader dispersion pattern near the substrate. While such behavior may be advantageous for large-area coating applications by increasing coating coverage, it may also compromise deposition resolution and thickness uniformity, particularly in applications requiring precise material placement and fine feature definition. Notably, increasing the gas pressure promoted particle focusing, resulting in a narrower dispersion pattern and a higher concentration of particles near the spray axis. This behavior can be attributed to the enhanced gas momentum and stronger particle acceleration at elevated pressures, which reduce particle divergence during transport. As such, higher-pressure conditions not only increase particle impact velocities but also improve particle focusing. On the other hand, increasing the gas temperature did not significantly influence particle focusing, as evidenced by the similar dispersion patterns observed when comparing the left- and right-hand sides of Fig. 4. This behavior is likely due to the fact that increasing temperature primarily enhances gas and particle velocities by increasing the thermal energy of the flow, while having a comparatively limited effect on the flow-field structure and aerodynamic forces governing particle trajectories. As a result, higher temperatures increase particle impact velocity but do not substantially alter particle dispersion or focusing behavior near the substrate. As such, inlet gas pressure has a more dominant influence on particle dispersion than gas temperature and must be carefully controlled to achieve the desired balance between particle focusing, coating uniformity, and spatial resolution.

The CFD results, shown in Fig. 5, are mapped into contour plots to provide a detailed visualization of the effects of process parameters (i.e., gas pressure, gas temperature) and particle size distribution on particle impact velocity. Specifically, the plots illustrate the variation in particle impact velocity as a function of gas temperature and particle diameter for both air and He carrier gases at inlet pressures of 4, 7, and 10 bar. Additional contour plots covering the full range of pressure

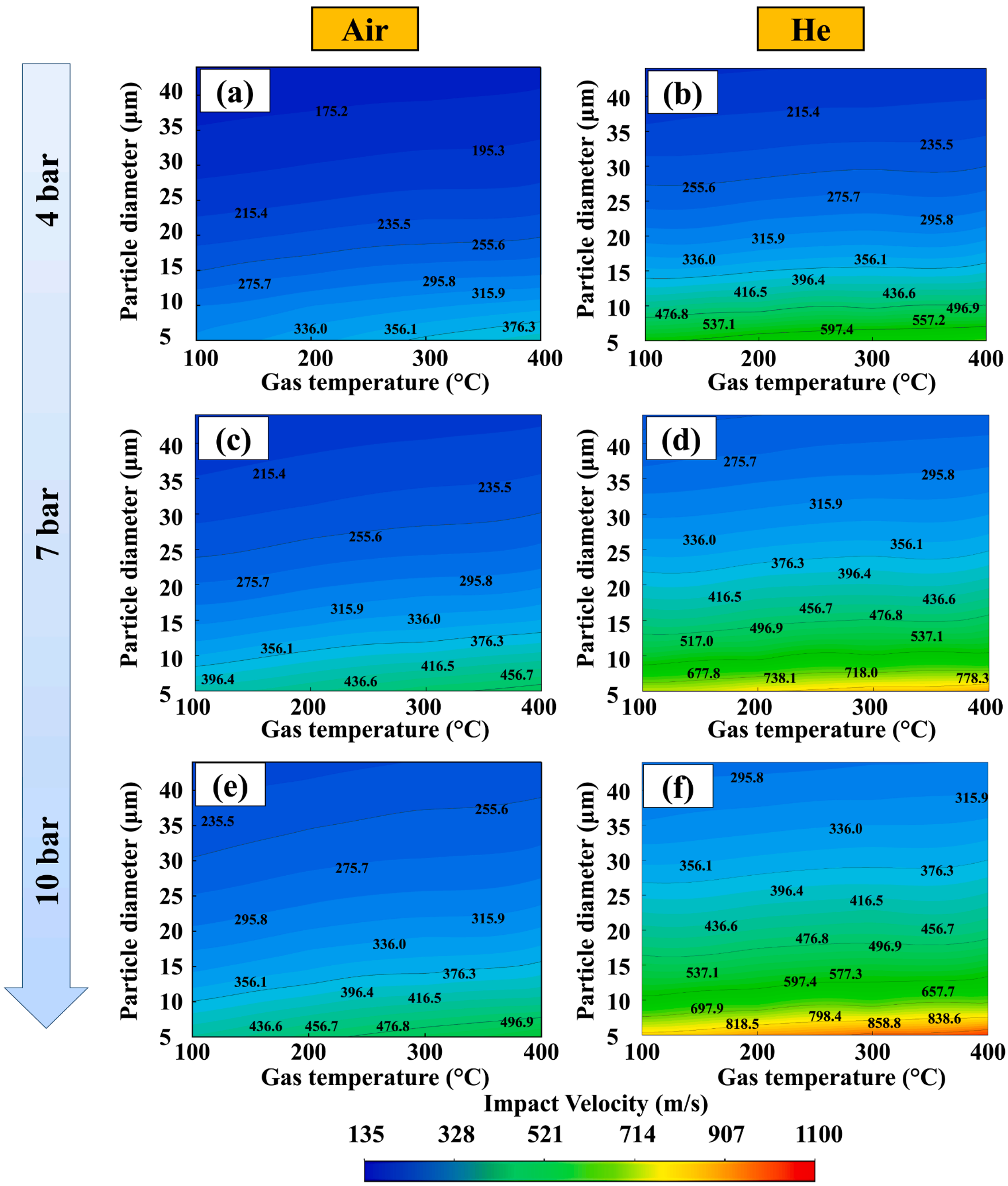

Fig. 5. Contour plots of particle impact velocity as a function of gas temperature and particle diameter for air and He at inlet pressures of 4, 7, and 10 bar.

conditions investigated in this study are provided in Figure S5 (Supporting Information). Smaller particles (<10 μm) were accelerated more effectively by the gas flow because of their lower inertia, resulting in substantially higher impact velocities. The highest impact velocities were observed for the particles (<10 μm) at elevated temperatures and pressures, whereas larger particles (>30 μm) exhibited significantly lower velocities due to their greater inertia. However, although smaller particles can reach higher impact velocities, they also exhibit higher critical velocities [45]. Thus, higher velocity does not necessarily ensure successful deposition, highlighting the importance of an appropriate particle size distribution [45]. Collectively, these results provide a comprehensive assessment of the combined effects of carrier gas type, operating conditions, and particle size on particle acceleration and impact behavior. Moreover, the generated dataset can serve as a valuable resource for researchers to identify suitable processing windows, estimate particle impact conditions for different feedstock size distributions, and support the optimization of the CSAM process for enhanced deposition performance.

4. Data-driven modeling results and discussions

4.1. Classification for deposition state

Figs. 6 and 7 provide a comprehensive evaluation of the machine learning classification models (i.e., LR, SVM, NN, RF) for predicting particle deposition behavior using the CFD-generated dataset. Fig. 6(a) compares the learning characteristics of the classification models, whereas Fig. 6(b) illustrates the corresponding deposition state distributions (i.e., deposition/no deposition) using ternary scatter plots. Fig. 7(a) depicts the three-dimensional decision boundaries, while

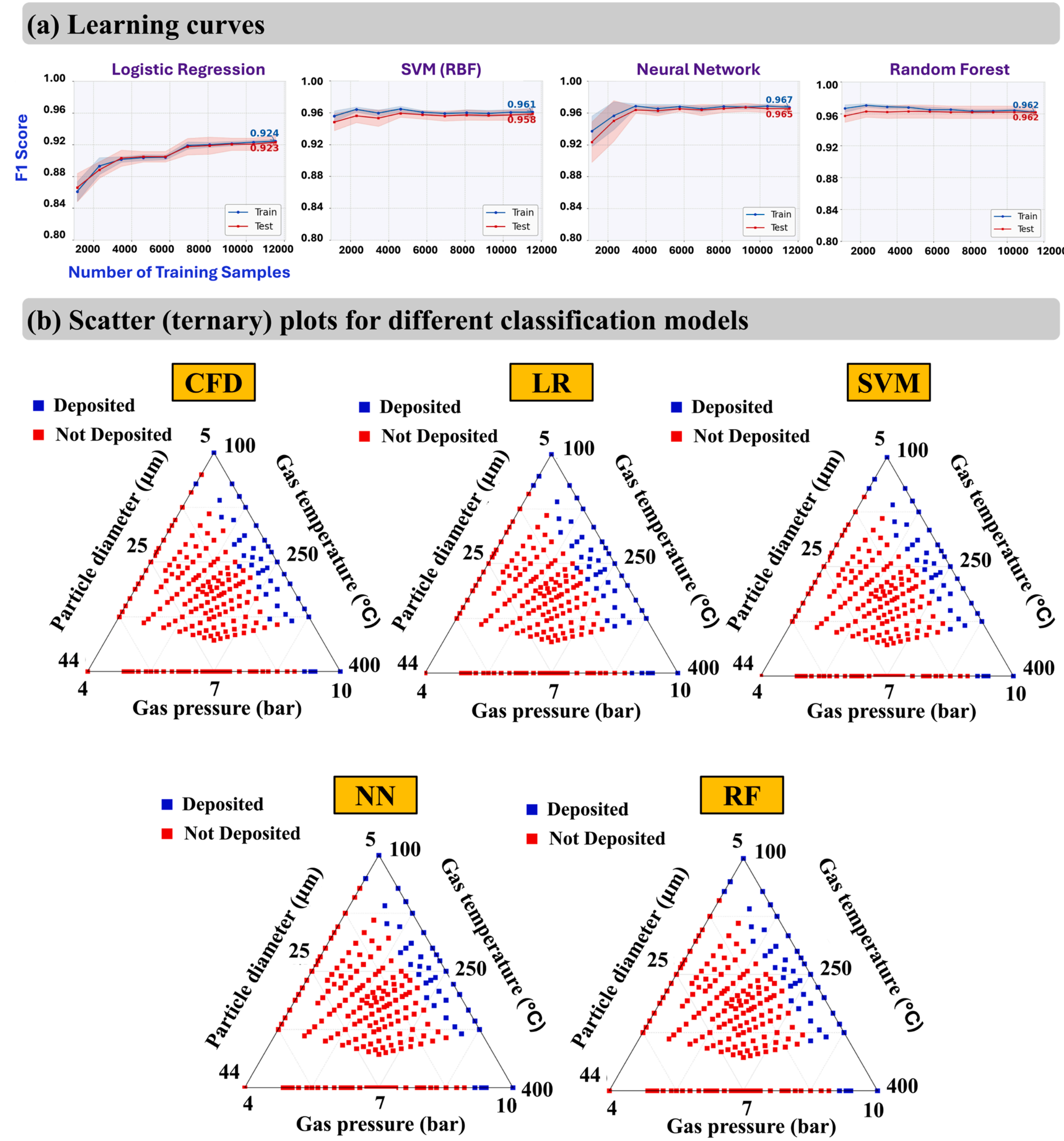

Fig. 6. Performance evaluation of classification models for deposition prediction: **(a)** learning curves, and **(b)** ternary scatter plots comparing CFD and ML predictions.

Fig. 7(b) summarizes the corresponding confusion matrices. Collectively, these results evaluate the predictive capability of the different classification models and provide a comprehensive comparison of their ability to reproduce the CFD-generated deposition behavior.

The learning curves shown in Fig. 6(a) demonstrate the learning performance of the four classification models as the training dataset size increases. For all models, the training and testing F1 scores remain closely matched throughout the training process, indicating good generalization capability and no significant evidence of overfitting. The learning curves also show that the model performance gradually stabilizes with increasing training dataset size, suggesting consistent convergence of the classification models. Among the four models, the NN achieved the highest training and testing F1 scores (0.967 and 0.965, respectively), followed closely by the RF and SVM models, whereas the LR model exhibited comparatively lower F1 scores (0.924 and 0.923, respectively). These results indicate that the nonlinear classification models provide a more accurate representation of the complex relationships among gas pressure, gas temperature, and particle diameter governing particle deposition than the linear LR model.

Fig. 6(b) compares the predicted deposition state distributions with the CFD-generated results. The classification models successfully reproduced the general deposition behavior observed in the CFD-generated dataset. Minor differences are primarily observed near the transition region separating deposition and non-deposition conditions, where

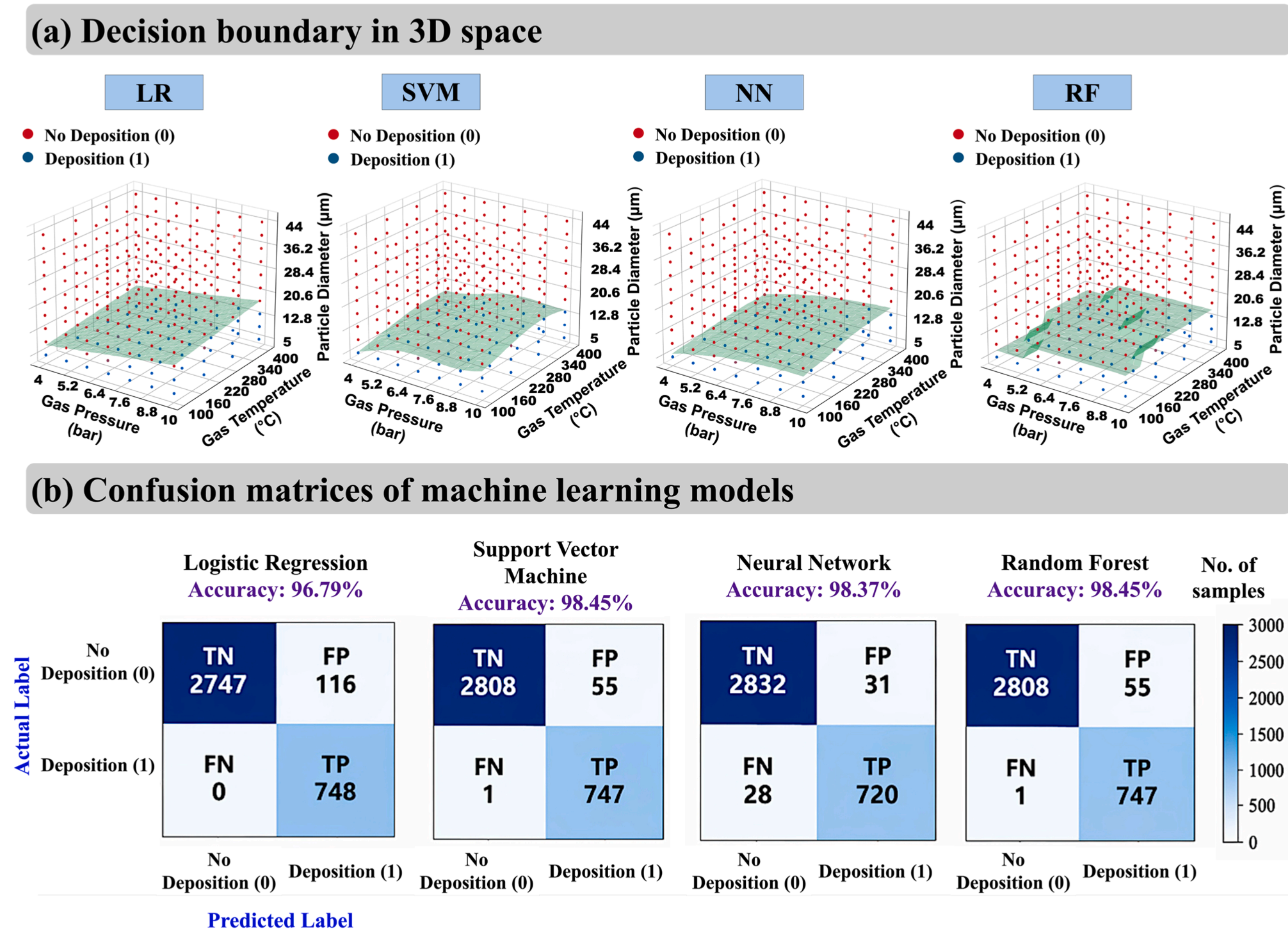

Fig. 7. Classification model evaluation for deposition prediction: (a) three-dimensional decision boundary visualization, and **(b)** confusion matrices of the ML models.

relatively small variations in the governing process parameters may alter the deposition state. Compared with the LR model, the SVM, NN, and RF models more accurately reproduced this transition boundary and exhibited closer agreement with the CFD-generated deposition distributions. These observations demonstrate that nonlinear classification algorithms are more effective in capturing the complex deposition characteristics obtained from the CFD simulations. Additional comparisons of the deposition probability contours predicted by the classification models are provided in the Supporting Information (Figure S6).

The predictive capability of the classification models is further assessed using the three-dimensional decision boundaries shown in Fig. 7(a) and the corresponding confusion matrices in Fig. 7(b). The decision-boundary plots show that the SVM, NN, and RF models more closely reproduced the nonlinear deposition boundary than the LR model, particularly within the transition region between deposition and non-deposition conditions. These observations are further supported by the confusion matrices, which show only a small number of misclassified samples for the nonlinear models. Among the four models, the SVM and RF achieved the highest classification accuracy (98.45%), followed closely by the NN model (98.37%), whereas the LR model achieved a comparatively lower accuracy of 96.79%. Overall, the excellent agreement between the CFD-generated deposition behavior and the ML predictions demonstrates that high-fidelity CFD simulations can be effectively integrated with ML to develop accurate surrogate models for particle deposition prediction. Once trained, these models can rapidly predict deposition behavior over a wide range of process conditions without requiring additional CFD simulations, thereby reducing the computational cost associated with repeated CFD simulations during process optimization.

4.2. Regression for deposition efficiency (DE)

Fig. 8 evaluates the predictive performance of the RR and GPR regression models for estimating DE. Fig. 8(a) compares the learning characteristics of the regression models, while Fig. 8(b) compares the corresponding DE contour distributions with the CFD-generated results. DE increased with increasing gas pressure and temperature, reaching ~30% at the upper limit of the investigated process window (i.e., $P = 10$ bar and $T = 400$ °C). Notably, these results correspond to low-pressure CS conditions, which generally yield lower DE than high-pressure CS systems [46,47]. Nevertheless, the predicted DE is consistent with the 20–30% range reported for low-pressure CS under comparable processing conditions [37,48], supporting the physical validity of the present simulations.

The learning curves shown in Fig. 8(a) demonstrate the predictive performance of the RR and GPR models as the training dataset size increases. The RR model exhibits relatively stable training and testing performance throughout the learning process, with the training performance consistently higher than the testing performance. In contrast, the GPR model exhibits a noticeable improvement in testing performance with increasing training data, resulting in closer agreement between the training and testing performance. Ultimately, the GPR model achieved higher training and testing R^2 values (0.951 and 0.896, respectively) than the RR model (0.928 and 0.882, respectively), indicating its

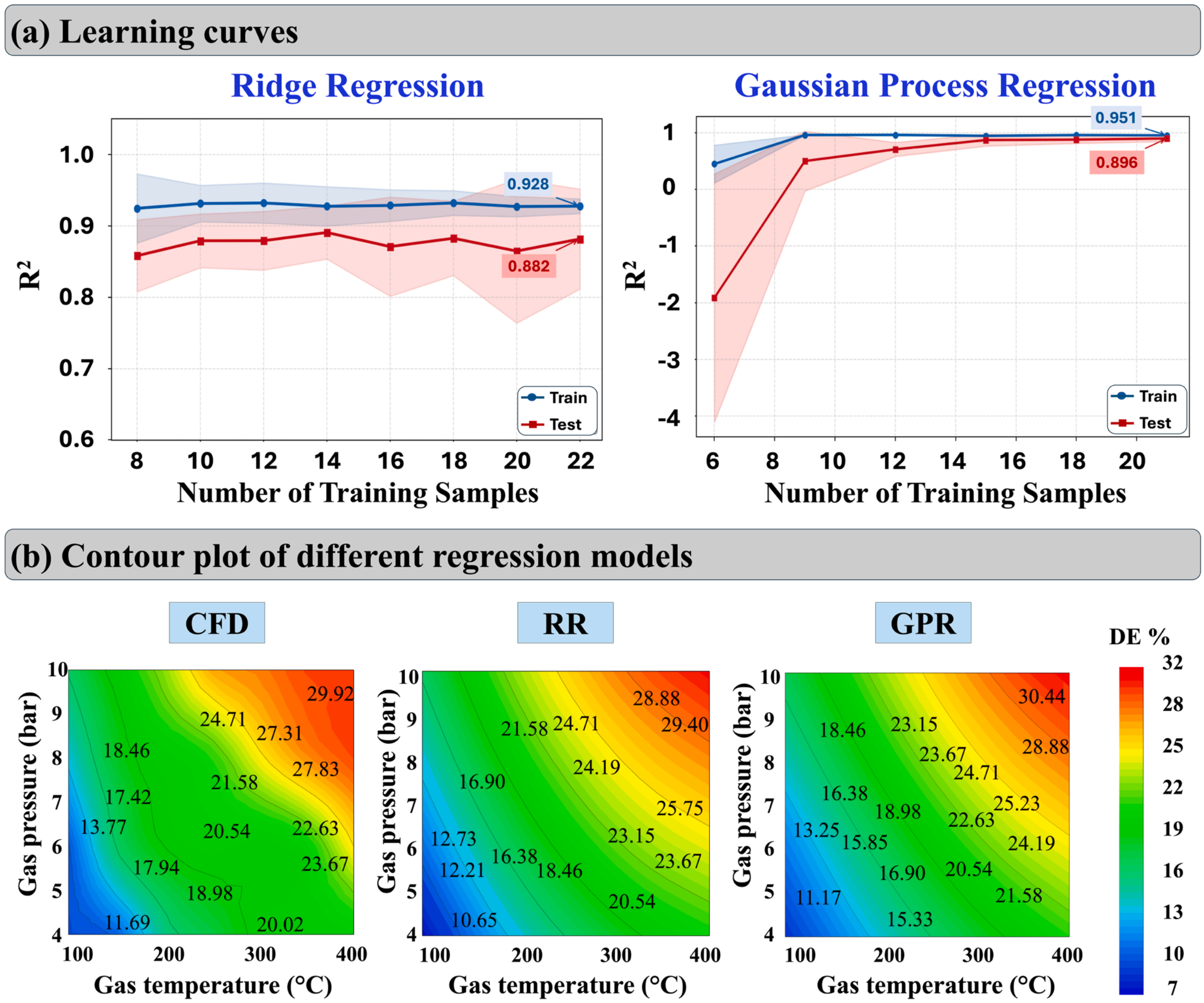

Fig. 8. Performance evaluation of regression models for deposition efficiency (DE) prediction: **(a)** learning curves, and **(b)** contour comparisons between CFD and machine learning predictions.

stronger capability to capture the nonlinear relationship governing deposition efficiency.

Fig. 8(b) compares the DE contour distributions predicted by the RR and GPR models with the CFD-generated results. Both regression models successfully reproduced the overall increase in DE with increasing gas pressure and gas temperature. However, noticeable differences are observed in their ability to reproduce the CFD-generated contour distributions. The RR model captured the general DE trend; however, its linear formulation resulted in comparatively smoother contour patterns and larger deviations from the CFD-generated distributions, particularly in regions exhibiting stronger nonlinear variations. In comparison, the GPR model more closely reproduced both the contour distributions and the DE values across the investigated parameter space, showing better agreement with the CFD-generated results in both the low- and high-DE regions. These observations indicate that the GPR model is more effective in capturing the nonlinear relationship between the governing process parameters and DE.

Overall, the GPR model outperformed RR in predicting DE by providing higher R^2 values and closer agreement with the CFD-generated contour distributions. These findings demonstrate that nonlinear regression provides a more reliable approach for modeling the complex relationship between gas pressure, gas temperature, and DE than conventional linear regression. Furthermore, the predicted DE contour distributions provide a practical guideline for process parameter selection by enabling the expected efficiency to be directly estimated over the investigated operating conditions. In addition, they facilitate the identification of suitable gas pressure and gas temperature combinations required to achieve the desired DE, thereby supporting efficient process optimization in CSAM.

5. Conclusion

This study developed a CFD-guided ML framework for predicting deposition behavior and DE in CSAM. CFD simulations and data-driven modeling were combined to investigate the effects of gas pressure, gas temperature and particle size on deposition characteristics. Various ML models were trained using the CFD-generated dataset, and their predictive performance was systematically evaluated and compared. Moreover, the results were mapped onto contour plots to visualize deposition regimes across the parameter space, providing practical process maps for identifying favorable processing windows and guiding process design and optimization. The important findings of the present study are summarized as follows:

- Increasing gas pressure and gas temperature significantly increased particle impact velocity and DE.

- He produced higher particle impact velocities than air, but resulted in greater particle dispersion. As such, although He can improve DE, it may reduce deposition resolution, which should be considered when selecting carrier gases for specific CSAM applications.
- Smaller particles (< 10 μm) attained higher impact velocities, while larger particles (30 – 44 μm) exhibited lower impact velocities due to their higher inertia and reduced responsiveness to gas acceleration.
- Among the classification models, SVM and RF achieved the highest deposition state prediction accuracy (98.45%), followed closely by the NN model (98.37%).
- The GPR model outperformed RR in capturing the nonlinear relationships governing DE, achieving a test R^2 of 0.896.

Beyond its predictive capability, the proposed CFD-guided ML framework can support the industrial implementation of CSAM by enabling rapid process-parameter screening while reducing repeated CFD simulations and experimental trial-and-error. Despite these benefits, the present study is limited to CFD-generated data and the investigated process window. Future work will therefore focus on expanding the dataset across broader operating conditions and incorporating additional experimental data. Physics-informed ML approaches will also be explored to integrate governing physical principles into the predictive framework, improving model accuracy, robustness, and generalizability.

CRediT authorship contribution statement

Fatema Tuj Zohora: Writing – original draft, Visualization, Validation, Methodology, Investigation, Data curation, Conceptualization; **Jaehun Jeon:** Writing – original draft, Validation, Methodology, Investigation, Formal analysis; **Semih Akin:** Writing – review & editing, Writing – original draft, Validation, Supervision, Resources, Project administration, Methodology, Investigation, Funding acquisition, Formal analysis, Conceptualization.

Declaration of competing interest

The authors declare that they have no known competing financial interests or personal relationships that could have appeared to influence the work reported in this paper.

Acknowledgments

The authors acknowledge the internal funding support from the Department of Mechanical, Aerospace, and Nuclear Engineering (MANE) at Rensselaer Polytechnic Institute (RPI).

Data availability

Data will be made available on request.

Supplementary material

Supplementary material associated with this article can be found in the online version at 10.1016/j.rineng.2026.112792.

References

[1] Y. Li, Y. Wei, X. Luo, C. Li, N. Ma, Correlating particle impact condition with microstructure and properties of the cold-sprayed metallic deposits, J. Mater. Sci. Technol. 40 (2020) 185–195.
[2] A. Nastic, B. Jodoin, D. Poirier, J.-G. Legoux, Particle temperature effect in cold spray: a study of soft particle deposition on hard substrate, Surf. Coat. Technol. 406 (2021) 126735.
[3] S. Dai, M. Cui, J. Li, M. Zhang, Cold spray technology and its application in the manufacturing of metal matrix composite materials with carbon-based reinforcements, Coatings 14 (7) (2024) 822.
[4] S. Yin, P. Cavaliere, B. Aldwell, R. Jenkins, H. Liao, W. Li, R. Lupoi, Cold spray additive manufacturing and repair: fundamentals and applications, Addit. Manuf. 21 (2018) 628–650.
[5] A. Kafle, R. Silwal, B. Koirala, W. Zhu, Advancements in cold spray additive manufacturing: process, materials, optimization, applications, and challenges, Materials 17 (22) (2024) 5431.
[6] G. Prashar, H. Vasudev, A comprehensive review on sustainable cold spray additive manufacturing: state of the art, challenges and future challenges, J. Clean. Prod. 310 (2021) 127606.
[7] H. Assadi, T. Schmidt, H. Richter, J.-O. Kliemann, K. Binder, F. Gärtner, T. Klassen, H. Kreye, On parameter selection in cold spraying, J. Therm. Spray Technol. 20 (6) (2011) 1161–1176.
[8] C. Zhang, T. Molla, C. Brandl, J. Watts, R. Mccully, C. Tang, G. Schaffer, Critical velocity and deposition efficiency in cold spray: a reduced-order model and experimental validation, J. Manuf. Process. 134 (2025) 547–557.
[9] X. Wang, F. Feng, M.A. Klecka, M.D. Mordasky, J.K. Garofano, T. El-Wardany, A. Nardi, V.K. Champagne, Characterization and modeling of the bonding process in cold spray additive manufacturing, Addit. Manuf. 8 (2015) 149–162.
[10] L. Alonso, M.A. Garrido-Maneiro, P. Poza, A study of the parameters affecting the particle velocity in cold-spray: theoretical results and comparison with experimental data, Addit. Manuf. 67 (2023) 103479.
[11] R.N. Raoelison, Y. Xie, T. Sapanathan, M.P. Planche, R. Kromer, S. Costil, C. Langlade, Cold gas dynamic spray technology: a comprehensive review of processing conditions for various technological developments till to date, Addit. Manuf. 19 (2018) 134–159.
[12] B. Samareh, A. Dolatabadi, A three-dimensional analysis of the cold spray process: the effects of substrate location and shape, J. Therm. Spray Technol. 16 (5) (2007) 634–642.
[13] R. Falco, K. Bobzin, H. Heinemann, M. Erck, K. Jasutyn, C. Wasels, S. Bagherifard, Integrating computational fluid dynamics and artificial intelligence for predicting in-flight thermo-kinetic properties in cold spray, J. Manuf. Process. 165 (2026) 461–471.
[14] C. Xia, C. Zhang, R. Li, A machine learning-based surrogate model for fast residual stress prediction in cold spray additive manufacturing, Addit. Manuf. Front. (2026) 200323.
[15] A. Habib, B. Javaid, Artificial intelligence and machine learning in cold spray additive manufacturing: a systematic literature review, J. Manuf. Mater. Process. 9 (10) (2025) 334.
[16] A.A. Citarella, L. Carrino, F. De Marco, L. Di Biasi, A.S. Perna, A. Viscusi, G. Tortora, AI data-driven optimization of cold spray coating manufacturing, IEEE Trans. Ind. Inf. 21 (2025) 7848–7858.
[17] A.S. Perna, A. Auriemma Citarella, F. De Marco, L. Di Biasi, A. Viscusi, G. Tortora, M. Durante, Optimizing cold spray deposition on thermoplastics: a machine learning approach focused on powder properties, J. Mater. Eng. Perform. 34 (8) (2025) 6527–6538.
[18] M. Eberle, S. Pinches, H. King, P. Guzman, K. Qin, A. Ang, Predicting deposition efficiency across diverse cold spray process parameters using machine learning, J. Therm. Spray Technol. 34 (5) (2025) 1642–1665.
[19] R. Falco, M. Jalayer, S. Bagherifard, Enhanced geometrical control in cold spray additive manufacturing through deep neural network predictive models, Virtual Phys. Prototyp. 20 (1) (2025) e2472388.
[20] L. Wang, M. Jadidi, A. Dolatabadi, A machine learning approach for predicting particle spatial, velocity, and temperature distributions in cold spray additive manufacturing, Appl. Sci. 15 (12) (2025) 6418.
[21] A. Hamrani, A. Medarametla, D. John, A. Agarwal, Machine-learning-driven optimization of cold spray process parameters: robust inverse analysis for higher deposition efficiency, Coatings 15 (1) (2024) 12.
[22] R.V. Savangouder, J.C. Patra, S. Palanisamy, A machine learning technique for prediction of cold spray additive manufacturing input process parameters to achieve a desired spray deposit profile, IEEE Trans. Ind. Inf. 20 (10) (2024) 12275–12283. https://doi.org/10.1109/TII.2024.3417300
[23] M. Eberle, S. Pinches, P. Guzman, H. King, H. Zhou, A. Ang, Application of machine learning for the prediction of particle velocity distribution and deposition efficiency for cold spraying titanium powder, Comput. Mater. Sci. 244 (2024) 113224.
[24] M. Eberle, S. Pinches, M. Osborne, K. Qin, A. Ang, Analysis of data generation and preparation for porosity prediction in cold spray using machine learning, J. Therm. Spray Technol. 33 (5) (2024) 1270–1291.
[25] R.H. Aparco, F. Tapia-Tadeo, Y.B. Ascarza, A.L. Ramírez, Y.-L. Huamán-Romaní, C.C. Otero, A machine learning approach for analyzing residual stress distribution in cold spray coatings, J. Therm. Spray Technol. 33 (5) (2024) 1292–1307.
[26] J. Lee, S. Akin, Y. Sim, H. Lee, E. Kim, J. Nam, K. Song, M.B.G. Jun, A stethoscope-guided interpretable deep learning framework for powder flow diagnosis in cold spray additive manufacturing, Manuf. Lett. 41 (2024) 1515–1525.
[27] Z. Wang, S. Cai, W. Chen, R.A. Ali, K. Jin, Analysis of critical velocity of cold spray based on machine learning method with feature selection, J. Therm. Spray Technol. 30 (5) (2021) 1213–1225.
[28] H. Canales, I.G. Cano, S. Dosta, Window of deposition description and prediction of deposition efficiency via machine learning techniques in cold spraying, Surf. Coat. Technol. 401 (2020) 126143.
[29] S. Rahman, S. Akin, Cold spray deposition of lunar regolith on polymeric substrates: a pathway toward in-situ resource utilization on the Moon, Surf. Interfaces 80 (2025) 108224.
[30] G. Huang, D. Gu, X. Li, L. Xing, H. Wang, Numerical simulation on syphonage effect of laval nozzle for low pressure cold spray system, J. Mater. Process. Technol. 214 (11) (2014) 2497–2504.
[31] O. Tregenza, N. Hutasoit, S. Palanisamy, C. Hulston, Air-based cold spray: an advanced additive manufacturing technique for functional and structural applications, Int. J. Adv. Manuf. Technol. 136 (11) (2025) 4677–4714.

[32] R.N. Raoelison, E. Aubignat, M.-P. Planche, S. Costil, C. Langlade, H. Liao, Low pressure cold spraying under 6 bar pressure deposition: exploration of high deposition efficiency solutions using a mathematical modelling, Surf. Coat. Technol. 302 (2016) 47–55.
[33] M. Abdelwahed, R. Bade, H. Chaker, M. Hassine, On the study of three-dimensional compressible Navier–Stokes equations, Bound. Value Probl. 2024 (1) (2024) 84.
[34] T. Gabor, S. Akin, M.B.-G. Jun, Numerical studies on cold spray gas dynamics and powder flow in circular and rectangular nozzles, J. Manuf. Process. 114 (2024) 232–246.
[35] C. Han, T. Gabor, H. Lee, J. Lee, S. Akin, M.B.-G. Jun, Pulsed cold spray system for physical unclonable function generation, Procedia CIRP 137 (2025) 176–180.
[36] T. Schmidt, H. Assadi, F. Gärtner, H. Richter, T. Stoltenhoff, H. Kreye, T. Klassen, From particle acceleration to impact and bonding in cold spraying, J. Therm. Spray Technol. 18 (5) (2009) 794–808.
[37] H. Li, Y. Le, H. Xu, Z. Li, Design of the dual-Path cold spray nozzle to improve deposition efficiency, J. Manuf. Mater. Process. 9 (5) (2025) 144.
[38] X.-J. Ning, Q.-S. Wang, Z. Ma, H.-J. Kim, Numerical study of in-flight particle parameters in low-pressure cold spray process, J. Therm. Spray Technol. 19 (6) (2010) 1211–1217.
[39] C.-Y.J. Peng, K.L. Lee, G.M. Ingersoll, An introduction to logistic regression analysis and reporting, J. Educ. Res. 96 (1) (2002) 3–14.
[40] G. Biau, E. Scornet, A random forest guided tour, Test 25 (2) (2016) 197–227.
[41] J. Schmidhuber, Deep learning in neural networks: an overview, Neural Netw. 61 (2015) 85–117.
[42] A.E. Hoerl, R.W. Kennard, Ridge regression: biased estimation for nonorthogonal problems, Technometrics 12 (1) (1970) 55–67.
[43] J. Wang, An intuitive tutorial to Gaussian process regression, Comput. Sci. Eng. 25 (4) (2023) 4–11.
[44] R.C. Dykhuizen, M.F. Smith, Gas dynamic principles of cold spray, J. Therm. Spray Technol. 7 (2) (1998) 205–212.
[45] R.F. Vaz, A. Garfias, V. Albaladejo, J. Sanchez, I.G. Cano, A review of advances in cold spray additive manufacturing, Coatings 13 (2) (2023) 267.
[46] R.F. Vaz, A. Silvello, J. Sanchez, V. Albaladejo, I.G. Cano, The influence of the powder characteristics on 316L stainless steel coatings sprayed by cold gas spray, Coatings 11 (2) (2021) 168.
[47] R.F. Vaz, A. Garfias, V. Albaladejo, J. Sanchez, I.G. Cano, How increasing cold spray coatings thickness affects their residual stress and properties, Surf. Coat. Technol. 485 (2024) 130867.
[48] K. Owusu Asamoah, D. Boruah, X. Zhang, M.E. Fitzpatrick, D. Khasraw, D. Rostohar, A review of portable low-pressure and medium-pressure cold spray repairs: process window, deposition behaviour, and deposit integrity, Surfaces 9 (3) (2026) 78.